Environ. Sci. Technol. 1991, 25, 268–274

Mechanisms of Inorganic Particle Formation during Suspension Heating of Simulated Aqueous Wastes

James A. Mulholland* and Adel F. Sarofim

Department of Chemical Engineering, 66-153, Massachusetts Institute of Technology, Cambridge, Massachusetts 02139

■ The fate of cadmium, lead, and nickel contained as nitrates in aqueous droplets was studied in a laboratory-scale furnace. Trimodal particle size distributions were observed. Metal partitioning between a residual mode (particle aerodynamic diameter, $D_{p,aero} > 7$ μm) and an intermediate mode (1 μm > $D_{p,aero} > 7$ μm) was consistent with the dependence of particle porosity on condensed-phase transformations during nitrate decomposition. In addition, ultrafine particles were produced. In the nickel experiments, where vaporization was not a reasonable mechanism for inorganic aerosol formation, it was found that 30–35% of the particles had aerodynamic diameters of less than 1 μm. Furthermore, a preponderance of cenospheres was observed in the large particle size fractions. It is conjectured that the fragmentation process of cenosphere bursting produced the submicron aerosol. In the cadmium and lead experiments, the amount of submicron particles produced was in qualitative agreement with the amount of metal oxide calculated to vaporize.

Introduction

Currently global natural fluxes of some metals, such as cadmium, are exceeded by anthropogenic fluxes (*1*). The emission of metal aerosols from incinerators represents a potential contribution to the anthropogenic sources. Recent field studies by the United States Environmental Protection Agency (EPA) and by European investigators have included measurements of metal emissions (*1–5*). Not only are the ultrafine particles produced during thermal decomposition difficult to capture by electrostatic precipitation (*6*), but these particles penetrate the deep lung when inhaled (*7*). In addition, increased metal emissions result from a rise in the concentration of metals in the major sinks of soil and water. Another reason for study of the fine inorganic particles generated by incinerators is that they provide a signature that can be used for source attribution. The amount and composition of ambient inorganic particulate matter varies widely with geographical location and time as a consequence of the wide variability of source emissions (*8*). Therefore, a mechanistic understanding of the physical and chemical processes governing inorganic particle formation during waste incineration is needed both for the development of better control technologies to reduce the contribution of inorganic aerosols to atmospheric pollution and for the development of better source allocation models that utilize ambient metal particulate markers.

Studies of the chemical and physical transformations of mineral matter in coal combustion have provided considerable insight into the formation of inorganic aerosols. It has been shown that coal fly ash is bimodally distributed with respect to size (*9–13*). The larger residual ash particles, with diameters in the range of 1–50 μm, contain trace amounts of volatile species concentrated at the particle surface. The submicron particles, on the other hand, are enriched with the more volatile coal mineral matter constituents (*10*). Laboratory studies (*11–13*) have shown that these particles are produced by the nucleation and subsequent coalescence and coagulation of a portion of the vaporized fly ash. Although the mass fraction of submicron particles is typically much less than that of the residual particles, the submicron particles are much more numerous and contain most of the particle surface area available for heterogeneous condensation of inorganic vapor; hence, volatile species enrichment is observed in the submicron particles.

While the subsequent processes of nucleation, condensation, coalescence, and coagulation govern the composition and size distribution within the submicron size mode, vaporization is largely responsible for the quantity of inorganic aerosol generated. Barton et al. have developed a metals-partitioning model based on equilibrium volatilization (*14*). Vaporization of inorganic species is complicated by simultaneous chemical processes such as decomposition, chlorination, oxidation, and reduction. For example, the vaporization of refractory oxides has been found to involve the more volatile suboxide or metal species as well as the oxide itself (*15*, *16*). Comparisons of the results of vaporization calculations with experimental and field measurements indicate that the equilibrium assumption is not always reasonable (*17*).

Char fragmentation has been shown to increase the number of residual ash particles, which increases particle surface area and, thus, particle vaporization rate (*18*). However, there is no evidence that fragmentation leads directly to submicron particle formation, with the exceptions of two explosive phenomena. First, Smith et al. (*19*) described a cenosphere formation and bursting phenomenon. Cenospheres are thin-walled hollow spheres formed by bubble nucleation and growth in a melt of critical viscosity. Raask (*20*) suggested that in coal-ash slag cenosphere formation, carbon monoxide is generated from iron carbide reacting with silica. The quantity of ash cenospheres formed in pulverized coal fired boilers varies with coal type, with as much as 5% being formed for some pyritic coals. If during cenosphere formation the viscosity of the melt is just below a critical value, Smith et al. suggested that the incipient cenosphere can burst, resulting in a shower of submicron fragments. A second mechanism known to produce submicron fragments is the so-called "secondary atomization" of liquid droplets. Lasheras et al. (*21*) have shown that, when multicomponent droplets of differing component liquid volatilities are heated rapidly, concentration gradients develop due to mass-transfer limitations. When heat transfer is great enough to vaporize the volatile-rich droplet core, disruptive burning occurs whereby the droplet explodes into tiny droplets. In liquids with dissolved inorganics this can lead directly to submicron aerosol formation.

To gain a better understanding of the mechanisms for metal partitioning between the fine condensation aerosol and the larger particles produced by the residue of metal-containing liquid wastes burned in suspension, a laboratory study was conducted. Effects of waste composition, waste atomization, local gas composition, and furnace temperature were measured (*22*). Three particle size modes were observed, and two pathways of submicron particle formation were hypothesized (Figure 1). This paper describes a subset of these experiments that most

 0013-936X/91/0925-0268$02.50/0

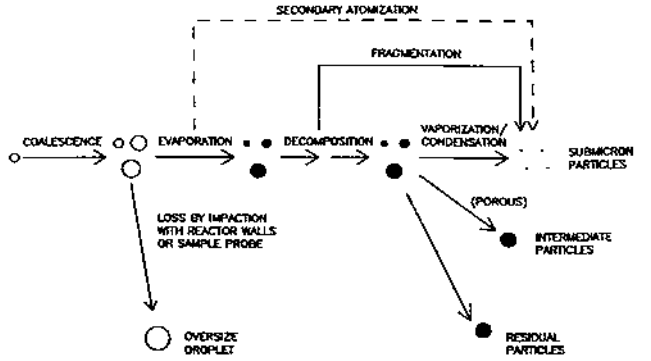

Figure 1. Pathways of inorganic particulate formation during suspension heating of metal-containing droplets (*22*). Droplet fragmentation by secondary atomization (dashed line) is not observed in experiments with metal compounds dissolved in pure solvents.

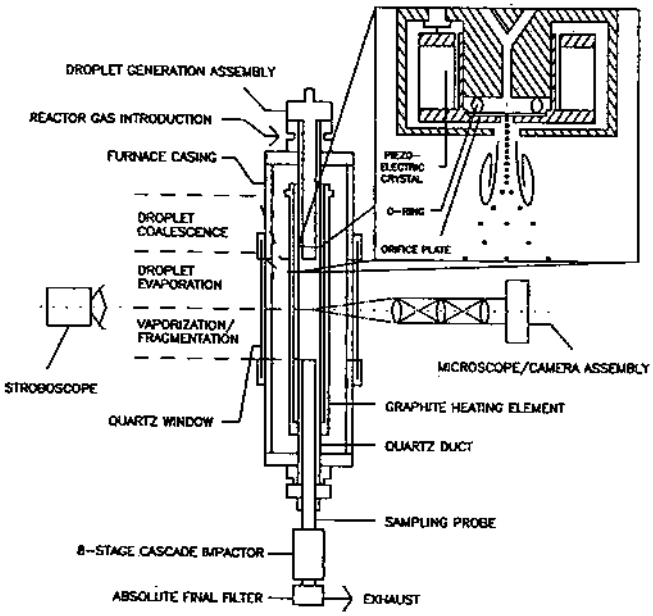

Figure 2. Drop-tube reactor with Berglund–Liu droplet generator, optical access for microphotography, and cascade impactor for particle size classification.

unambiguously demonstrates the roles of decomposition, explosive fragmentation, and vaporization in the formation of inorganic particles.

Experimental Section

Apparatus and Methods. A laminar flow, isothermal drop-tube furnace was used to vaporize aqueous droplets containing nitrates of cadmium, lead, and nickel. The general features of the laboratory-scale facility are shown in Figure 2. A stream of monodisperse droplets, generated by a Berglund–Liu-type device (*23*), is injected down the center of the reaction zone contained by an electrically heated quartz tube (47 mm i.d.). The full reaction zone length is 33 cm, representing a nominal bulk gas residence time of 1.4 s. A metered flow rate (6.0 standard L/min) of dry air is preheated to the furnace wall temperature prior to entry into the reaction zone. In the present set of experiments, furnace wall temperatures ranging from 900 to 1500 K were maintained.

Optical access to the entire reaction zone provides the ability to evaluate droplet atomization quality by microphotography. Satellite dropets are virtually eliminated by operating the Berglund–Liu device at an optimum vibrational frequency. Droplets of uniform size, with less than 10% standard deviation in measured diameter, are produced (*22*). Secondary atomization due to differences in droplet component volatilities was neither expected nor observed in these experiments with a single solvent. Secondary atomization by Coulombic explosions was also avoided in these experiments. Calculations show that the electrostatic charge induced during droplet generation is substantially less than the limit imposed by the Rayleigh stability criterion over the entire lifetime of the droplet. Thus, droplet atomization processes are not responsible for heterogeneity in the emitted particle size distribution.

The entire product stream is recovered and rapidly quenched by dilution gas. Particle deposition in the collection probe is avoided by transpiring gas radially through the probe's inner wall. The particles and gases are then passed through an Anderson Mark II cascade impactor for on-line aerodynamic size classification of particles between 0.4 and 15 μm. Impaction stages are greased to minimize particle bounce. The particles with aerodynamic diameter less than 0.4 μm pass through the impactor and are collected on an absolute final filter.

Each solution studied contained one metallic salt additive. The use of single metal solutes obviates the need for detailed chemical analysis of the collected particles; gravimetric analysis provides the particle aerodynamic size distribution directly. Inversion and smoothing of the data are performed by using the algorithm of Markowski (*24*). Scanning electron microscopy (SEM) of the larger size fractions is utilized to provide information concerning particle morphology.

Metals Studied. Cadmium, lead, and nickel compounds were chosen for study both because these metals are of highest priority in EPA's proposed regulations (*25*) and because they incorporate a wide range of volatilities. Cadmium is a refractory oxide, with a sublimation point of 1832 K for the oxide and a boiling point of 1038 K for the pure metal. Lead oxide boils at 1745 K, whereas lead metal boils at 2013 K. Nickel oxide and nickel metal both have boiling points of about 3000 K. Nitrates of cadmium [$Cd(NO_3)_2{\cdot}4H_2O$], lead [$Pb(NO_3)_2$], and nickel [$Ni(NO_3)_2{\cdot}6H_2O$] were dissolved into distilled water in a mass concentration of 1.5%. Each metal salt solution was studied separately, allowing for simple gravimetric analysis of the collected particulates. The lack of strongly exothermic reactions that would accompany organometallic decomposition and vaporization allows for simple calculation of droplet and particle temperatures. During thermal treatment the nitrate decomposes to the thermodynamically favored monoxide. Treating the collected particles in bulk as the monoxide resulted in a mass balance closure to within 5%.

Transformations between solid and liquid phases also occur. Of critical importance is the condensed-phase viscosity during the release of nitrogen dioxide and oxygen. Adapted from the observations on changes in drying droplets at ambient gas temperatures above decomposition by Charlesworth and Marshall (*26*), Figure 3 shows sequences of physical transformations during decomposition of different types of droplets. Lead nitrate decomposes by sublimation; hence, its decomposition might be depicted by sequence I. Cadmium nitrate decomposes as a low-viscosity liquid; sequence II describes such a transformation. Nickel nitrate is a viscous melt during decomposition; sequence III represents a transformation path of this type.

Droplet and Incipient Particle Size Distributions. A 20 μm diameter orifice is vibrated at 215 kHz to produce a steady stream of 36 μm diameter droplets with an initial interdroplet spacing of 2.7 diameters. However, due to rapid deceleration of droplets in a linear array, droplet

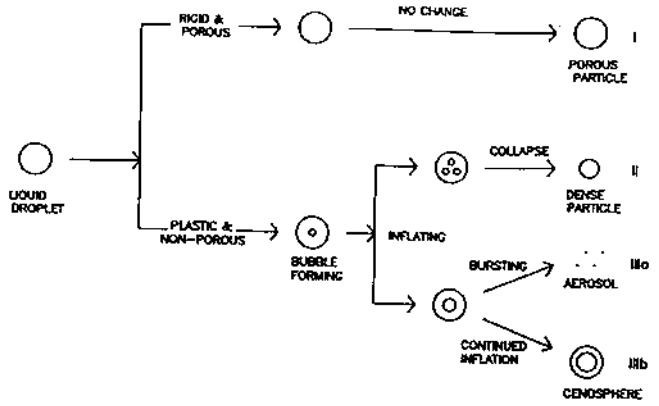

Figure 3. Physical transformations in droplets at ambient gas temperatures above the decomposition temperature, adapted from the observations on changes in drying droplets by Charlesworth and Marshall (*26*).

collisions and coalescence ensue, resulting in the development of a heterogeneous size distribution. Droplet size distributions are measured in situ by microphotography, with details given elsewhere (22). After only 3 cm (about 2 ms) of flight, the mean droplet diameter has increased by 70%. To avoid further droplet collisions and coalescence, dispersion gas is introduced coaxially with the droplets, resulting in a dilute spray being developed. Microphotographs show that droplet size growth due to coalescence ceases after 3 cm. Therefore, the measured droplet size distribution at this location is used as a starting point in the vaporization calculations, with droplet collisions assumed to be negligible beyond this point. This distribution was found to be bimodal, with multiplets consisting of 75% of the total number of droplets. From this starting distribution measurement, the number of oversize droplets (i.e., droplets with diameters greater than 100 μm) that are calculated to pass through the reaction zone without completely evaporating is consistent with the number observed (1.5% by number, corresponding to approximately 15% by mass).

The decay of the homogeneous droplet size distribution generated, due to the aforementioned droplet interaction effects, results in a heterogeneous size distribution of incipient particles. The minimum initial particle diameter for these experiments, produced from a singlet drop, is 4 μm. This corresponds to an aerodynamic diameter (referenced to spherical geometry and unit density) of approximately 8 μm. The average initial particle diameter is a factor of 1.7 greater than this minimum initial diameter.

Results and Discussion

Particle Size Distribution Measurements. In Figure 4 particle aerodynamic size distributions are shown for the heating of the nickel, cadmium, and lead solutions. The histograms shown represent the measured masses on each of the eight cascade impactor stages and on the final filter; the curves represent results from the deconvolution of the data. From the left column of Figure 4 it is seen that data inversion and smoothing did not alter qualitatively the

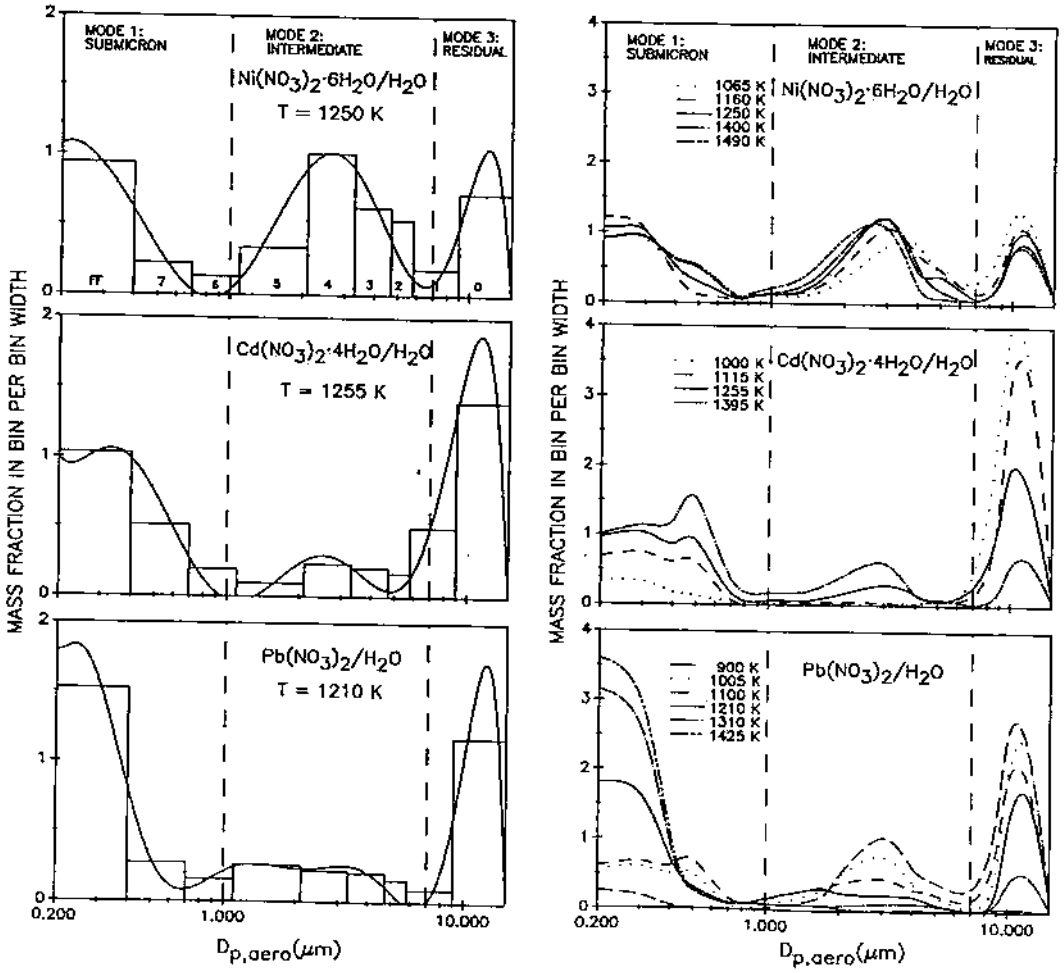

Figure 4. Aerodynamic particle size distributions. The graphs in the left column include the actual cascade impactor stage data in histogram form and a regression fit to the output of the data inversion code for one furnace temperature. The graphs in the right column show the results from the inversion algorithm without regression for several furnace temperatures.

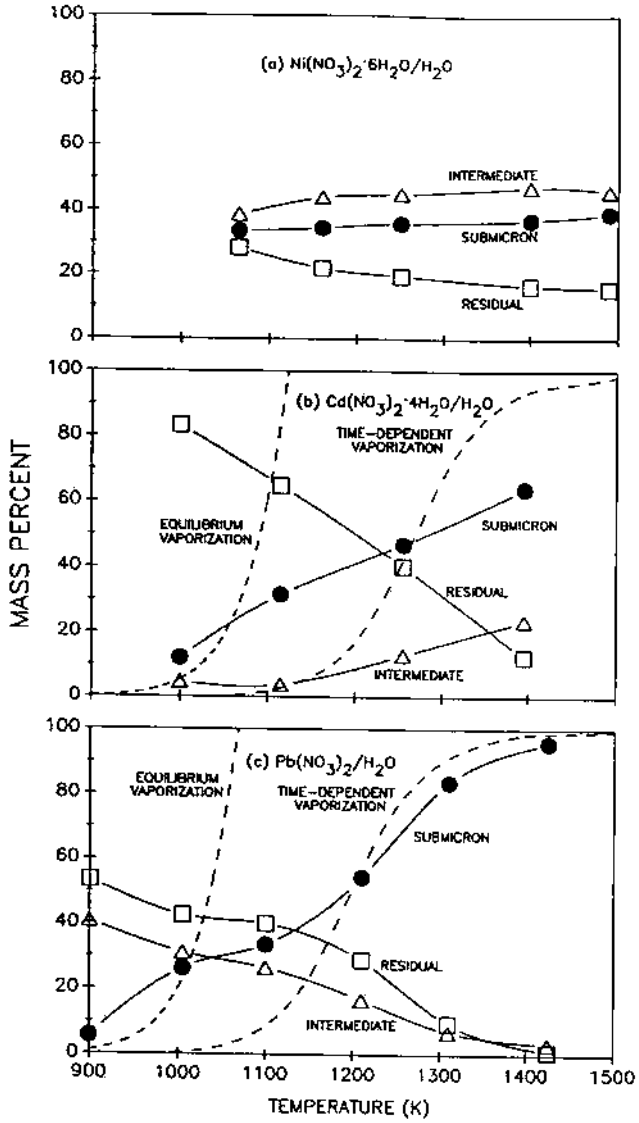

Figure 5. Mass fraction measurements by aerodynamic particle size mode, with time-dependent calculations shown for the vaporization of the metal monoxides.

trend of the original data. However, the shape of the calculated distribution near the upper and lower diameter end points is arbitrary.

The data exhibit a trimodel character when displayed in a semilogarithmic plot of mass fraction versus aerodynamic diameter. The aerodynamic diameters marking mode boundaries are less than 1 μm (submicron mode), between 1 and 7 μm (intermediate mode), and greater than 7 μm (residual mode). All of the particles produced following droplet evaporation are initially of residual mode size.

The integrated mass percents of metal oxide collected in each of the three modes of the aerodynamic size distribution are shown in Figure 5 as functions of furnace temperature for the nickel, cadmium, and lead nitrate solutions studied. Also shown are the equilibrium (based on furnace volumetric flow rate) and time-dependent (based on a model described in Appendix A) vaporized mass percents of CdO and PbO (dashed lines). Equilibrium and time-dependent values of vaporization of NiO are insignificant at temperatures below 2000 K.

Nickel oxide submicron particle mass fractions of 35–40% were measured over the temperature range studied (Figure 5a). It is unlikely that any of these submicron particles could have formed via a vaporization route due

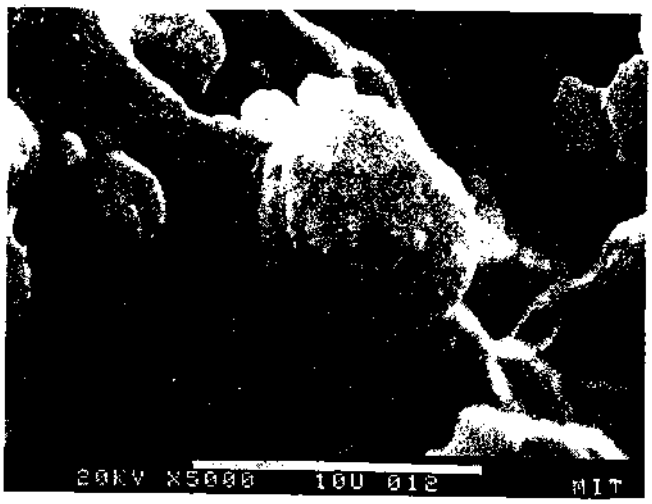

Figure 6. SEM photograph of a typical nickel oxide cenosphere.

to the extremely low volatility of nickel and its oxides. In addition, the almost total lack of dependence of submicron particle fraction on temperature suggests that vapor pressure is not a driving force.

Submicron particles formed by vaporization and condensation and residual particles formed by the unvaporized component of each droplet had been expected prior to the start of this study (22). However, an unexpected intermediate particle size mode is seen, most distinctly for nickel. One possible explanation is that of a varying particle porosity created during decomposition and phase transformation, as presented in Figure 3. Droplet size distribution heterogeneity results in particles ranging in initial size by a factor of 3. In addition, the larger droplets require longer times to evaporate, leaving little or no time available for exposure of the particles to the reactor gases. Thus, variations in particle porosity arise due to variations in incipient particle size and subsequent particle residence time. The inertial impaction parameter that determines aerodynamic size classification is proportional to the particle density times its actual diameter squared. For particles of equal mass and composition but differing density, the inertial impaction parameter and, therefore, the particle aerodynamic diameter, is proportional to density raised to the one-third power (and, likewise, inversely proportional to actual diameter). Thus, the net effect of increased porosity on aerodynamic size classification is a decrease in aerodynamic diameter. The amount of particles of intermediate size relative to the amount of particles in the residual size category is greatest for nickel, less for lead, and least for cadmium, consistent with the order of particle porosity as hypothesized in Figure 3.

SEM Analysis. Direct evidence of the particle porosity variation between metal compounds suggested by the particle size distribution measurements was obtained by SEM analysis of the residual and intermediate particles. Nickel oxide residual and intermediate particles were found to contain a large fraction of cenospheres. A typical cenosphere had a diameter of 5–10 μm, a shell thickness of about 0.5 μm, and a single blow hole (Figure 6). A second observation from SEM analysis was that the residual and intermediate particles of cadmium had smaller optical diameters than did the particles of lead with equivalent aerodynamic diameter. This suggests that the particles of lead oxide, which has a greater bulk density, are more porous than the cadmium oxide particles. Thus, the formation of particles of intermediate size is consistent with the direct observation of extremely porous nickel cenospheres and the inferred observation of moderate

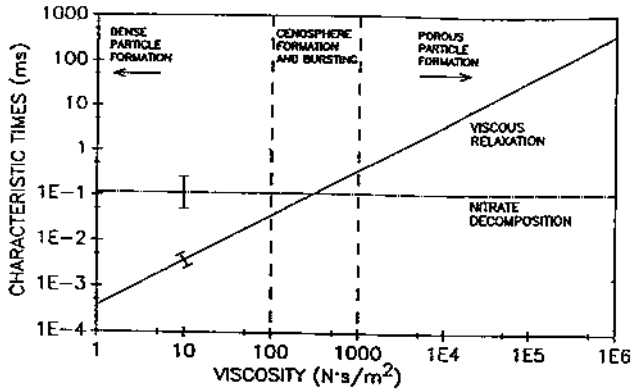

Figure 7. Characteristic viscous relaxation time for a 4-μm particle expanding to 10 μm. Also shown is the characteristic time for nitrate decomposition (dashed–dotted line) for a 4-μm particle at a furnace temperature of 1200 K. Variations in the results of calculations using a wide range of metal nitrate properties are indicated by error bars.

porosity in the lead particles relative to the dense cadmium particles.

As already stated, the particles produced after water evaporation vary in initial size and reactor residence time due to the heterogeneity of the droplet size distribution. This affects the dynamics of nickel oxide cenosphere formation. The submicron mass fraction of nickel particles can be attributed to the cenosphere bursting phenomenon reported by Smith et al. (*19*). A fraction of the particles with the necessary size and residence time characteristics may produce cenospheres that burst into submicron fragments. A first attempt to develop a method of predicting the critical energetics for cenosphere formation and bursting follows.

A simple criterion is hypothesized for qualitative prediction of particle transformations during nitrate decomposition. During decomposition of the nickel nitrate to the oxide, the release of nitrogen dioxide and oxygen in the core of the viscous melt results in bubble nucleation and growth. By use of the expression for the rate of expansion of a hollow sphere derived by Goodier (*27*) (Appendix A), the characteristic times for cenosphere formation are estimated for a 4-μm particle (Figure 7). A D^2 law estimate of nitrate decomposition time is also shown in Figure 7 (dashed–dotted line). Cenosphere formation and bursting is expected to occur when the viscous relaxation time is of the same order of magnitude as the characteristic time of nitrate decomposition. This criterion suggests that a critical viscosity of between 10^2 and 10^3 N·s/m^2 is required for cenosphere formation, consistent with the critical viscosity reported by Raask (*28*). When the viscosity during decomposition is sufficiently low such that the viscous relaxation time is much less than the nitrate decomposition time, as in the case of cadmium nitrate decomposition, the gas bubble escapes before the shell hardens. As a result, a dense particle forms. When the viscous relaxation time is much greater than the nitrate decomposition time, a porous particle results.

This order of magnitude analysis is useful if measurements of melt viscosities during decomposition are available. If measurements are not available, estimates may be made from the inorganic compound melting point and its viscosity dependence on temperature (usually assumed to be exponential). Obviously, the melt viscosity varies as the composition varies. However, due to the wide variability of viscosity for different chemical compounds, identification of compounds likely to form dense particles, cenospheres, or porous particles can be made with this analysis using a minimum value of viscosity, i.e., using the viscosity attained at the onset of decomposition.

Vaporization Calculations. To estimate the amount of metal that vaporizes, a pseudo-steady-state model of transient heating and vaporization is used (*29*), assuming infinitely fast chemical decomposition of the nitrate to the monoxide (Appendix B). Coupled with the equations for spherically symmetric mass and energy transfer is the one-dimensional momentum transport equation, derived from a balance of the drag and gravitational forces. These equations, valid for both the droplet and particle processes, are solved numerically to yield time-dependent vaporization rates, given initial droplet size and velocity distributions and composition, and given gas temperature, flow rate, and composition.

The calculation of metal vaporization provides only a qualitative match with the measurement of submicron particle fraction (Figure 5b and c). The heterogeneity of the initial droplet size distribution has the effect of broadening the dependence of vaporization on temperature, but not to the extent observed. Moreover, at the lower temperatures studied, the amount of submicron particles formed exceeds the amount that would be formed if the vapors were saturated in cadmium and lead oxides. Therefore, while the primary mechanism of submicron particle formation in the cadmium and lead tests appears to be that of vaporization, it is likely that fragmentation contributed to submicron particle formation as well.

Conclusion

The aerodynamic particle size distributions produced by the rapid heating of polydisperse droplet streams were measured for aqueous solutions containing cadmium, lead, and nickel nitrates over a range of furnace temperatures from 900 to 1500 K. The particle size distributions were found to be trimodal. Variations in particle porosity for the three metal compounds studied appear to account for the differences in the distribution of particles with aerodynamic diameter greater than 1 μm. SEM analysis of the larger nickel oxide particles revealed a preponderance of cenospheres. Nearly independent of temperature, a large fraction of submicron particles was produced in the nickel tests, suggesting that cenosphere bursting occurred. Submicron particle formation in the cadmium and lead tests is in qualitative agreement with the vaporization of cadmium and lead oxides. However, fragmentation may also contribute to submicron cadmium and lead particle formation, particularly at the lower temperatures studied. Direct measurements of the fine particle size distribution are needed to support or reject this hypothesis.

Appendix A. Viscous Relaxation Time Calculations

With the expression for the rate of expansion of a hollow sphere derived by Goodier (*27*), the characteristic time for cenosphere formation can be estimated from

$$dr/dt = r^2\Delta p/(4\eta L_{sh}) \qquad \text{(A1)}$$

where $\Delta p = p - [p_a + 2\sigma(1/r + 1/r_i)]$. For the purposes of illustration, calculations of viscous relaxation time as a function of viscosity were made for a particle of 4-μm diameter forming a cenosphere of 10-μm diameter (Figure 7). A bubble pressure transient given by an instantaneous gas mass release and resulting in a final pressure equal to the equilibrium pressure is assumed. The characteristic time was calculated as the time required for the particle to expand to 95% of its final size. A nominal surface tension of 0.3 N/m^2 was used, with the sensitivity to a 50% change indicated by an error bar.

Appendix B. Vaporization Model

After injection, a droplet undergoes heating and evaporation, followed by particle heating, chemical decomposition, and phase transformation. To predict the amount of metal that vaporizes, the processes of coupled droplet heating and evaporation followed by coupled metal monoxide heating and vaporization are modeled. Other processes (e.g., metal nitrate decomposition, melting, and solidification) are neglected. A pseudo-steady-state model of droplet and particle vaporization is used. In the condensed phase, with the uniform internal temperature assumption (i.e., infinite thermal diffusivity limit)

$$c_{pc}\rho_c(dT_c/dt) = [6k\mathrm{Nu}(T - T_c)/D^2] + (3\rho_c\Delta H_{vap}/D)(dD/dt) \quad \text{(B1)}$$

In the gas phase, assuming steady state, spherical symmetry, a Lewis number of unity, constant properties, and no chemical reaction, the heat and mass transport conservation equations (Fourier's law and Fick's law, respectively) become identical. For small mass-transfer rates, one obtains

$$dm/dt = -(\pi\rho_c D^2/2)(dD/dt) = k_{xm}\pi D^2\{(p_A - p_A^\infty)/(1 - p_A)\} \quad \text{(B2)}$$

where the mass-transfer coefficient is given by $k_{xm} = \rho D_{AB}\mathrm{Sh}/D$. The vapor pressure of species A is given by the Clausius–Clapeyron equation: $p_A = \exp[-\Delta H_{vap}(T_{bp}/T_c - 1)/(R_A T_{bp})]$. Applying film theory to derive a correction factor for high rates of mass transport (*29*), one obtains

$$(dm/dt)^* = \theta(dm/dt) \quad \text{(B3)}$$

where the correction factor is given by $\theta = [\ln(1 + B)]/B$. The mass-transfer number is given by $B = c_p(T - T_c)/\Delta H_{vap}$. Forced convection effects are accounted for by an empirical correction to the heat- and mass-transfer coefficients (*29*). Coupled with the mass- and energy-transfer equations is the one-dimensional momentum transport equation, derived from a balance of the drag and gravitational forces.

$$dv_c/dt = -[3\rho/(4\rho_c D)]C_D v_r^2 + g \quad \text{(B4)}$$

These equations, valid for both the droplet and particle processes, are solved numerically to yield time-dependent vaporization rates for the droplet and particle, given an initial droplet size and velocity distribution and composition, and given a gas temperature, flow rate, and composition.

Glossary

B	mass transfer number
c_p	gas specific heat, J/g·K
c_{pc}	condensed-phase specific heat, J/g·K
C_D	drag coefficient
D	droplet/particle diameter, μm
$D_{p,aero}$	particle aerodynamic diameter, μm
D_{AB}	mass diffusivity, cm^2/s
g	gravitational constant, 981 cm/s^2
ΔH_{vap}	latent heat of vaporization, J/g
k	gas thermal conductivity, J/cm·s·K
k_{xm}	mass-transfer coefficient, g/cm^2·s
L_{sh}	cenosphere shell thickness, μm
dm/dt	mass vaporization rate (low values), g/s
$(dm/dt)^*$	mass vaporization rate (high values), g/s
Nu	Nusselt number
p	cenosphere internal pressure, atm
Δp	actual and equilibrium pressure difference, atm
p_a	furnace ambient pressure, atm
p_A	vapor pressure of species A, atm
p_A^∞	partial pressure of species A in bulk gas, atm
r	radius, μm
r_i	cenosphere inner radius, μm
R_A	specific gas constant, J/g·K
Sh	Sherwood number
t	time, s
T	bulk gas temperature, K
T_c	condensed-phase temperature, K
T_{bp}	boiling point temperature, K
v_c	condensed-phase velocity, cm/s
v_r	relative velocity between gas and droplet, cm/s
η	absolute viscosity, $N\text{-}s/m^2$
θ	correction factor for high mass-transfer rates
ρ	gas density, g/cm^3
ρ_c	condensed-phase density, g/cm^3
σ	surface tension, N/m^2

Literature Cited

(1) Brunner, P. H.; Monch, H. *Waste Manage. Res.* **1986**, *4*, 105.
(2) Trenholm, A. R.; Garg, S.; Licis, I. Particulate, Metal, and Organic Emissions from a Hazardous Waste Incinerator. Paper presented at the Air and Waste Management Association Specialty Conference on Thermal Treatment of Municipal, Industrial, and Hospital Wastes II, Pittsburgh, PA, November 7–10, 1989.
(3) Vogg, H.; Braun, H.; Metzger, M.; Schneider, J. *Waste Manage. Res.* **1986**, *4*, 65.
(4) Gounon, J.; Milhau, A. *Waste Manage. Res.* **1986**, *4*, 95.
(5) Kauppinen, E. I.; Pakkanen, T. A. *Atmos. Environ.* **1990**, *24A*, 423.
(6) Ondor, J. M.; Ragaini, R. C.; Biermann, A. H. *Environ. Sci. Technol.* **1979**, *13*, 946.
(7) Task Group on Lung Dynamics. *Health Phys.* **1966**, *12*, 173.
(8) Hidy, G. M. *Aerosols: An Industrial and Environmental Science*; Academic Press: Orlando, FL, 1984; Chapter 7.
(9) Sarofim, A. F.; Howard, J. B.; Padia, A. S. *Combust. Sci. Technol.* **1977**, *16*, 187.
(10) Natusch, D. F. S.; Wallace, J. R.; Evans, C. A. *Science* **1974**, *183*, 202.
(11) Taylor, D. D.; Flagan, R. C. *Aerosol Sci. Technol.* **1982**, *1*, 103.
(12) Linak, W. P.; Peterson, T. W. *Aerosol Sci. Technol.* **1984**, *3*, 77.
(13) Helble, J. J.; Sarofim, A. F. *J. Colloid Interface Sci.* **1989**, *128*, 348.
(14) Barton, R. G.; Clark, W. D.; Seeker, W. R. *Proceedings of the First International Congress on Toxic Combustion Byproducts*; *Combust. Sci. Technol.*, in press.
(15) Neville, M.; Sarofim, A. F. In *Nineteenth Symposium (International) on Combustion*; The Combustion Institute: Pittsburgh, PA, 1982; pp 1441–9.
(16) Quann, R. J.; Sarofim, A. F. In *Nineteenth Symposium (International) on Combustion*; The Combustion Institute: Pittsburgh, PA, 1982; pp 1429–40.
(17) Seeker, W. R. Waste Combustion. Invited paper presented at the Twenty-Third International Symposium on Combustion, Orleans, France, July 22–27, 1990.
(18) Helble, J. J.; Sarofim, A. F. *Combust. Flame* **1989**, *76*, 183.
(19) Smith, R. D.; Campbell, J. A.; Nielson, K. K. *Atmos. Environ.* **1979**, *13*, 607.
(20) Raask, E. *J. Inst. Fuel* **1968**, *41*, 339.
(21) Lasheras, J. C.; Fernandez-Pello, A. C.; Dryer, F. L. *Combust. Sci. Technol.* **1980**, *22*, 195.
(22) Mulholland, J. A.; Yue, G.; Sarofim, A. F. The Formation of Inorganic Particles during Suspension Heating of Simulated Wastes. *Environ. Prog.*, in press.
(23) Berglund, R. N.; Liu, B. Y. H. *Environ. Sci. Technol.* **1973**, *7*, 147.
(24) Markowski, G. R. *Aerosol Sci. Technol.* **1987**, *7*, 127.
(25) *Fed. Regist.* 40 CFR Parts 260-271 [FLR-3153-5]. Burning of Hazardous Waste in Boilers and Industrial Furnaces,

Proposed Rule; U.S. Environmental Protection Agency. *Fed. Regist.* **1987**, *52* (No. 87), pp 16982–17050 (May 6).
(26) Charlesworth, D. H.; Marshall, W. R. *AIChE J.* **1960**, *6*, 9.
(27) Goodier, J. N. *Philos. Mag.* **1936**, *22*, 678.
(28) Raask, E. *Mineral Impurities in Coal Combustion*; Hemisphere: New York, 1985; p 132.
(29) Bird, R. B.; Stewart, W. E.; Lightfoot, E. N. *Transport Phenomena*; John Wiley & Sons: New York, 1960; pp 648–67.

Received for review May 17, 1990. Revised manuscript received September 6, 1990. Accepted September 17, 1990. The research reported was performed under EER Corporation Subcontract 8560-49, under EPA Prime Contract 68-02-4247.